Contemporary Mathematics
https://ojs.wiserpub.com/index.php/CM/

Research Article

Numerical Solutions for Boundary Value Problem of Mixed Convection Flow Inside a Rectangular Cavity with Heated Obstacles

Adel Alblawi[1], Sohail Nadeem[2,3]*

[1]Mechanical Engineering Department, College of Engineering, Shaqra University, Dawadmi, P.O., 11911, Saudi Arabia
[2]Department of Mathematics, Quaid-I-Azam University, 45320, Islamabad, 44000, Pakistan
[3]Department of Mathematics, Wenzhou University, China
E-mail: sohail@qau.edu.pk

Received: 7 July 2025; **Revised:** 1 September 2025; **Accepted:** 15 October 2025

Abstract: The mixed convection flow and heat transfer in a vented rectangular hollow with an adiabatic enclosure and an interior solid obstruction that generates heat are investigated numerically. The combined effects of natural convection, which is produced by the heat-generating obstruction, and forced convection, which is facilitated by an exit port at the top of the right wall and an intake port at the bottom of the left wall, propel the flow. The Galerkin Finite Element Method (GFEM) is used to solve the governing equations for mass, momentum, and energy. The findings are examined to comprehend the intricate relationship between the Grashof number (Gr), which controls buoyant strength, and the Reynolds number (Re), which controls forced flow inertia. The average Nusselt number (Nu) and the average fluid temperature inside the cavity are used to quantify the total heat transfer performance, while streamlines and isotherms are used to depict the flow patterns and thermal distributions. The results show that the Re-Gr combination has a significant impact on the flow structure and thermal performance. This study offers vital information for improving the thermal design of devices including heat exchangers, solar thermal collectors, and electronic cooling enclosures.

***Keywords*:** Finite Element Method (FEM) solutions, mixed convectional flow, rectangular cavity, heated obstacles

MSC: 65L05, 34K06, 34K28

Abbreviation

u, v	Velocity components	(ms^{-1})
p	Pressure	(Pa)
θ	Temperature	(K)
μ	Dynamic viscosity	(kg/ms)
k	Thermal conductivity	(W/mK)
c_p	Specific heat at constant pressure	(J/kgK)
ν	Kinematic viscosity	(m^2/s)
ρ	Density	(kg/m^3)

DOI: https://doi.org/10.37256/cm.7120267758

β	Coefficient of thermal expansion	(K^{-1})
θ_c	Fluid's temperature	(K)
g	Gravity	(ms^{-2})
U_0	Velocity component	(ms^{-1})
ρ_0	Fluid's density at θ_c	($kg{\cdot}m^{-3}$)
L	Length	(m)
U, V	Dimensionless velocity components	(-)
τ	Dimensionless time	(-)
†	Dimensionless temperature	(-)
P	Dimensionless pressure	(-)
Re	Reynolds number	(-)
Nu	Nusselt number	(-)
Gr	Grashof number	(-)
Pr	Prandtl number	(-)

1. Introduction

The study of heat transfer within enclosures and hollows is decisive for a widespread variety of engineering and everyday sciences. Researchers have used theoretical, experimental and numerical methods to discover convection flow and thermal behaviour in various geometries, including rectangular, hexagonal, and triangular cavities with different types of heating and obstruction. The Finite Element Method (FEM) has been particularly useful for analyzing complex geometries and boundary conditions. Recognizing heat transfer within enclosures is fundamental for designing and optimizing electronic equipment, solar receivers, and other systems that rely on heat exchange. Employing theoretical, experimental, and numerical methods, we have studied convection flow and thermal properties in various cavities and enclosures. Many researchers in this field have conducted extensive research. Guo and Sharif [1] studied mixed convection heat transfer using a rectangular two-dimensional hollow with an intensively heated bottom wall with isothermal boundaries and continuously moving vertical wall. Enclosure driven by a partially flexible divider and internal heat generation, Selimefendigil and Oztop [2] explored mixed convection in a viscous fluid subject to convective heating. Haq et al. [3] examined the cavity that results from mixed convection partially driven by a semi-heated wall, whereas Gangawane et al. [4] examined it when a lid-driven cavity is present. Haq et al. [5] achieved forced convection with a two-dimensional trapezoidal cavity connected to a partially lid-driven trapezoidal lid with ovate cold obstacle awareness should be oval-shaped cold obstacle placement.

Moallemi and Jang [6] presented their findings on how the Reynolds number influenced the thermal performance of a lid-driven square hollow. The effect of Reynolds and Grashof numbers on mean Nusselt numbers was explored independently by Prasad and Kosef [7]. By adjusting Reynolds and Grashof numbers, Khanafer and Chamkha [8] and Basak et al. [9] made comparable observations on the performance of mixed convection. By integrating bioconvection and Magnetohydrodynamics (MHD), Nadeem et al. [10] offer computational research on the behavior of motile microorganism suspensions in ferrofluid flow. Using a two-phase flow technique, the model investigates the impact of magnetic fields, interactions between nanoparticles, and swimming microorganisms. Important discoveries include changed flow dynamics at different magnetic intensities and increased thermal conductivity brought on by microbial motility. By changing the Reynolds number while maintaining the Grashof number constant, the impact of the Richardson number was investigated by Dagtekin and Oztop [11]. In a lid-driven chamber, Richardson number was used to characterize the regime of heat transfer in mixed convection system. In a curved channel, Alblawi et al. [12] examined the MHD-driven ciliary flow of a Casson nanofluid containing carbon nanotubes while taking slip effects and metachronal wave motion into account. By employing low Reynolds number and long wavelength approximations, they obtained exact solutions for temperature and velocity profiles while examining the effects of variables such as the nanoparticle volume fraction and Hartmann number. The results indicate that nanoparticles lower velocity close to the right wall, but that magnetic and

curvature effects raise temperature. The work offers important new information on the behavior of nanofluids in ciliary transport-related biomedical and engineering applications.

We used a variety of heated obstacles to boost the heat transfer efficiency. Ullah et al. [13] exploited a partially heated rectangular chamber to investigate the thermal and optical properties of CuO-water nanofuid. The flow field in the cavity is imperiled to two heated wavy rods. By utilizing a triangle-shaped heated wall and a square hollow, Alsabery et al. [14] demonstrated nanomaterial mixed convection flow. In their investigation of Buongiorno's nanofluid model across a coiled exponentially stretched surface, Alblawi et al. [15] examine the combined impacts of curvature, thermophoresis, and Brownian motion. As the curvature parameter (K) increases, the results show improved heat transmission; however, with higher thermophoresis (Nt), the thickness of the thermal boundary layer decreases. Khan and Khan [16] investigated thermophysical characteristics of nanofluids in a triangular hollow with an adiabatic pentagonal obstruction. Hamid et al. [17] undertake numerical simulations in lid-driven cavity for mixed convection flow with circular obstructions on left and right sides. Using a trapezoidal chamber with two cylindrical heated barriers placed inside, Khan et al. [18] investigated two-dimensional flow and heat transfer. Addressing microscale heat transfer, Nikan et al. [19] presented an efficient computational method for the hyperbolic heat conduction equation in thin metal films. Their results confirm the model's accuracy in simulating non-classical thermal wave propagation and predicting elevated temperature distributions. The fluid flow in a chamber with multiple heated barriers was investigated by Usman et al. [20].

One of the numerical issues of estimating convective heat fluxes within enclosed regions clarifies the governing parameters. The complexity of computations and governing boundary conditions and so on are some of the stumbling blocks. The FEM has been used to investigate constraints of heat transmission in hexagonal chambers with heated fences. Haq et al. [21] evaluated parameters of heat transmission in hexagonal chambers with partially heated wall using finite element analysis. Abdelmalek et al. [22] applied FEM to investigate convective heat transfer in cavity containing a wavy spherical heater. A localized meshfree collocation approach is presented by Nikan et al. [23] in their work on the telegraph equation for electrical signal transmission. Their approach outperforms conventional finite element approaches in terms of computing efficiency and numerical precision, handling complicated geometries with ease and exhibiting great accuracy in simulating signal distortion and attenuation. Rehman et al. [24] studied impacts of heated triangular spars formed by elliptical obstacles. Using a finite element approach, Kargarsharifabad [25] examined the properties of the insulated obstruction in the cavity. Li et al. [26] demonstrated the great accuracy and computing efficiency of their localized meshless collocation approach for simulating turbulent flows in 2D Burgers-type equations. Their technology offers a potent substitute for conventional mesh-based techniques, drastically lowering computing costs while preserving high agreement with analytical results. A useful starting point for a more thorough examination of the applications is the [27–44] section, which provides some current studies in this area.

Our study's objective is to numerically analyze fluid flow and heat transmission in a rectangular hollow with four thermal barriers: two on lower side fence and two on upper fence as shown in Figure 1. There is only one inlet and one outlet in the chamber. The inlet is in bottom left bend, and outflow is positioned at top right corner. The side walls are chilly, whereas the upper and lower walls are adiabatic. The barrier locations were selected to (i) improve flow mixing throughout the cavity, (ii) guarantee symmetric heating effects, and (iii) enable comparison with earlier cavity studies that employed obstacles positioned at corners or mid-walls. The empirical solution is obtained using mathematical model based on PDEs. The numerical analysis of mixed convection in a cavity with four heated barriers, a configuration that is seldom described. Our approach uses the Galerkin Finite Element Method (GFEM) to investigate complicated thermal-fluid interactions by combining the effects of Reynolds and Grashof numbers with obstacle-induced heat production in a novel way. Analyzing the combined effect of buoyancy and inertia forces, showing how many impediments affect convection patterns and heat transmission, and offering fresh perspectives on how to optimize thermal systems through geometric adjustments are some of the main contributions. This paper's remaining sections are arranged as follows: The governing equations and mathematical modeling of the physical problem are shown in Section 4. While Section 6 describes the numerical solution approach, Section 5 presents the non-dimensionalization process. The finite element formulation is described in Section 7, and the findings are thoroughly discussed in Section 8, along with how Reynolds and Grashof numbers affect the flow and heat transfer properties. Section 9 concludes by summarizing the main findings and outlining potential avenues for further research.

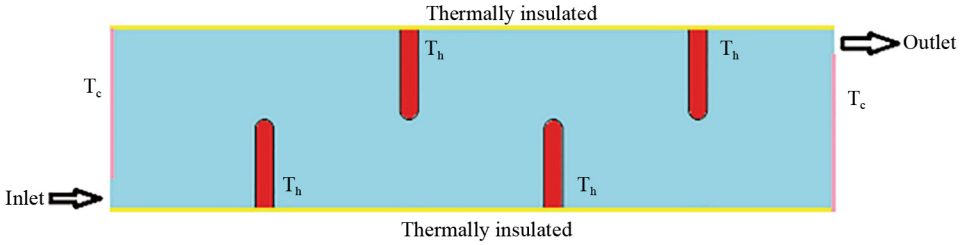

Figure 1. Geometry of cavity

2. Mathematical modeling

The physical issue is seen in such a manner that the cavity's length is measured along the x-axis and its height is measured along the y-axis. Both velocities are bidimensional and, in the case of an unstable flow, will also depend on t. The $\dot{u}$, $\dot{v}$ components of the velocity are located along the x-axis, and y-axis respectively. The upper and lower boundaries are thermally insulated, and four obstacles are at higher temperatures than the side walls. We will explore temperature distribution and velocity profiles for $1 \leq Re \leq 50$ and $10^3 \leq Gr \leq 10^5$. The working fluid's thermophysical characteristics are assumed to be constant at a reference temperature in this investigation. This popular simplification [1, 9] separates the effects of Reynolds and Grashof numbers and lowers computing costs. These results are illustrative of fluids with minor property changes, even if actual characteristics alter with temperature. Temperature-dependent features ought to be included in future research.

The principal equations in component form can be expressed as follows in dimensional form [45]:

$$\frac{\partial \dot{u}}{\partial x} + \frac{\partial \dot{v}}{\partial y} = 0, \tag{1}$$

$$\left(\frac{\partial \dot{u}}{\partial t} + \dot{u}\frac{\partial \dot{u}}{\partial x} + \dot{v}\frac{\partial \dot{u}}{\partial y}\right) = -\frac{1}{\rho}\frac{\partial p}{\partial x} + \nu\left(\frac{\partial^2 \dot{u}}{\partial x^2} + \frac{\partial^2 \dot{u}}{\partial y^2}\right), \tag{2}$$

$$\left(\frac{\partial \dot{v}}{\partial t} + \dot{u}\frac{\partial \dot{v}}{\partial x} + \dot{v}\frac{\partial \dot{v}}{\partial y}\right) = -\frac{1}{\rho}\frac{\partial p}{\partial y} + \nu\left(\frac{\partial^2 \dot{v}}{\partial x^2} + \frac{\partial^2 \dot{v}}{\partial y^2}\right) + g\beta(\theta - \theta_c), \tag{3}$$

$$\frac{c_p}{\kappa}\left(\frac{\partial \theta}{\partial t} + \dot{u}\frac{\partial \theta}{\partial x} + \dot{v}\frac{\partial \theta}{\partial y}\right) = \frac{1}{\kappa}\left(\frac{\partial^2 \theta}{\partial y^2} + \frac{\partial^2 \theta}{\partial x^2}\right). \tag{4}$$

Boundary conditions are for $\dot{t}$,

$$\dot{\theta} = 0, \quad \dot{u} = 0, \quad \dot{v} = 0, \qquad \text{for } 0 \leq \dot{x}, \dot{y} \leq L,$$

for $\dot{t} > 0$,

$$\dot{\theta} = 0, \quad \dot{u} = 0, \quad \dot{v} = 0, \qquad \text{for } 0 \leq \dot{x}, \dot{y} \leq L,$$

$$\dot{\theta} = \dot{\theta}_c, \quad \dot{u} = \dot{U}_0, \quad \dot{v} = 0, \qquad \text{at } \dot{x} = 0,$$

$$\dot{\theta} = \dot{\theta}_c, \quad \frac{\partial \dot{u}}{\partial \dot{x}} = 0, \quad \frac{\partial \dot{v}}{\partial \dot{y}} = 0, \qquad \text{at } \dot{x} = L, \tag{5}$$

$$\frac{\partial \dot{\theta}}{\partial \dot{y}} = 0, \qquad \text{at } \dot{y} = 0 \quad \& \quad \dot{y} = \frac{L}{4},$$

$$\dot{\theta} = \dot{\theta}_h, \qquad \text{for obstacles (A, B, C, D).}$$

3. Dimensionless procedure

Scaling transformations are used to non-dimensionalize the dimensional governing equations (Eqs. (1)-(4)), producing the dimensionless variables shown below:

$$X = \frac{x}{L}, \quad Y = \frac{y}{L}, \quad U = \frac{u}{U_0}, \quad V = \frac{v}{U_0},$$

$$t = \frac{t\mu}{\rho L^2}, \quad P = \frac{p}{\rho U_0^2}, \quad \theta = \frac{\theta - \theta_c}{\theta_h - \theta_c}.$$

Under this parametrization, eqs. (1)-(4) become:

$$\frac{\partial U}{\partial X} + \frac{\partial V}{\partial Y} = 0, \tag{6}$$

$$\frac{\partial U}{\partial t} + U\frac{\partial U}{\partial X} + V\frac{\partial U}{\partial Y} = -\frac{\partial P}{\partial X} + \frac{1}{Re}\left(\frac{\partial^2 U}{\partial X^2} + \frac{\partial^2 U}{\partial Y^2}\right), \tag{7}$$

$$\frac{\partial V}{\partial t} + U\frac{\partial V}{\partial X} + V\frac{\partial V}{\partial Y} = -\frac{\partial P}{\partial Y} + \frac{1}{Re}\left(\frac{\partial^2 V}{\partial X^2} + \frac{\partial^2 V}{\partial Y^2}\right) + \frac{Gr}{Re^2}\theta, \tag{8}$$

$$\frac{\partial \theta}{\partial t} + U\frac{\partial \theta}{\partial X} + V\frac{\partial \theta}{\partial Y} = \frac{1}{Re \cdot Pr}\left(\frac{\partial^2 \theta}{\partial X^2} + \frac{\partial^2 \theta}{\partial Y^2}\right), \tag{9}$$

where

$$Gr = \frac{g\beta L^3 \Delta\theta}{\nu^2}, \quad Re = \frac{U_0 L}{\nu}, \quad Pr = \frac{\mu c_p}{k}, \quad \nu = \frac{\mu}{\rho}, \quad \Delta\theta = \theta_h - \theta_c,$$

for $t = 0$,

$$\theta = 0, \quad U = 0, \quad V = 0, \quad \text{for} \quad 0 \leq X, Y \leq 1,$$

for $t > 0$,

$$\begin{aligned} &\theta = 0, \quad U = 1, \quad V = 0, \quad \text{at} \quad X = 0, \\ &\theta = 0, \quad \frac{\partial U}{\partial X} = 0, \quad \frac{\partial V}{\partial X} = 0, \quad \text{at} \quad X = 1, \\ &\frac{\partial \theta}{\partial Y} = 0, \quad \text{at} \quad Y = 0 \quad \& \quad Y = 1, \\ &\theta = 1, \quad \text{for obstacles (A, B, C, D).} \end{aligned} \tag{10}$$

4. Method of solution

Numerical approaches are employed to solve the momentum and energy equations since analytical methods fail in various instances. The convergence behavior for the linear grid (G7) is depicted in Figure 2. Solving the system of equations (6)-(9) by consuming the Galerkin finite element technique subject to supposed boundary conditions, as previously mentioned in COMSOL Multiphysics (6.1). Applying the penalty finite element approach the pressure in the modelled system is penalized by the penalty parameter provided as

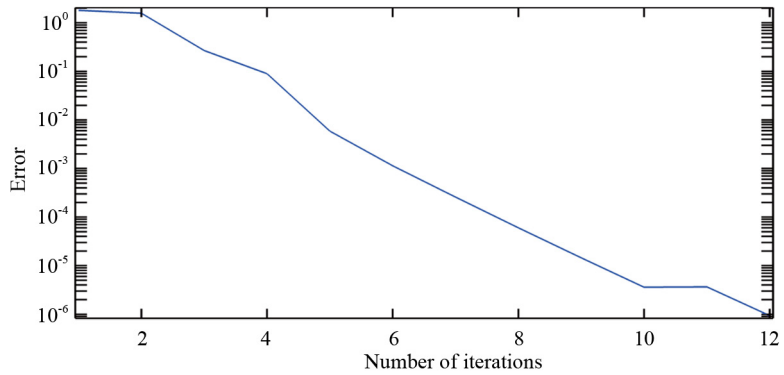

Figure 2. Convergence plot at selected grid size G7

$$\dot{P} = -\gamma \left(\frac{\partial \dot{U}}{\partial x} + \frac{\partial \dot{V}}{\partial T} \right). \tag{11}$$

Using Eq. (11) in Eq. (7)-(8)

$$\dot{U}\frac{\partial \dot{U}}{\partial x}+\dot{V}\frac{\partial \dot{U}}{\partial T}=\gamma\left(\frac{\partial^2 \dot{U}_i}{\partial x^2}+\frac{\partial^2 \dot{V}_i}{\partial x\,\partial t}\right)+\frac{1}{Re}\left(\frac{\partial^2 \dot{U}}{\partial x^2}+\frac{\partial^2 \dot{V}_i}{\partial T^2}\right), \tag{12}$$

$$\dot{U}\frac{\partial \dot{U}}{\partial x}+\dot{V}\frac{\partial \dot{U}}{\partial T}=\gamma\left(\frac{\partial^2 \dot{U}_i}{\partial x\,\partial t}+\frac{\partial^2 \dot{V}_i}{\partial T^2}\right)+\frac{1}{Re}\left(\frac{\partial^2 \dot{V}}{\partial x^2}+\frac{\partial^2 \dot{V}_i}{\partial T^2}\right)+\frac{\Omega r}{Re^3}\overline{V}. \tag{13}$$

The weak formulations of Eqs. (12), (13) and (9) on the element of δ_m with the weight functions w_1, w_2 and w_3 are

$$\int_{\Delta_{Am}} w_1\left(U\frac{\partial U}{\partial x}+V\frac{\partial U}{\partial T}\right)\mathrm{d}\mathbf{A}-\int_{\Delta_{Am}} w_1\gamma\left(\frac{\partial^2 \dot{U}}{\partial x^2}+\frac{\partial^2 \dot{V}}{\partial x\,\partial t}\right)\mathrm{d}\mathbf{A}-\int_{\Delta_{Am}} w_1\frac{1}{Re}\left(\frac{\partial^2 \dot{U}}{\partial x^2}+\frac{\partial^2 \dot{V}}{\partial T^2}\right)\mathrm{d}\mathbf{A}=0, \tag{14}$$

$$\begin{aligned}&\int_{\Delta_{Am}} w_2\left(U\frac{\partial^2 \dot{U}}{\partial x}+V\frac{\partial U}{\partial T}\right)\mathrm{d}\mathbf{A}-\int_{\Delta_{Am}} w_2\gamma\left(\frac{\partial^2 \dot{U}}{\partial x\,\partial t}+\frac{\partial^2 \dot{V}}{\partial T^2}\right)\mathrm{d}\mathbf{A}\\&-\int_{\Delta_{Am}} w_2\frac{1}{Re}\left(\frac{\partial^2 \dot{V}}{\partial x^2}+\frac{\partial^2 \dot{V}}{\partial T^2}\right)\mathrm{d}\mathbf{A}-\frac{\alpha c}{Re^3}\int_{\Delta_{Am}} w_2\bar{t}\,\mathrm{d}\mathbf{A}=0,\end{aligned} \tag{15}$$

$$\int_{\Delta_{Am}} w_3\left(\frac{\partial^2}{\partial t}+U\frac{\partial^2 \bar{t}}{\partial x}\right)\mathrm{d}\mathbf{A}-\frac{1}{Re\,\alpha\,r_t}\int_{\Delta_{Am}} w_4\left(\frac{\partial^2 \bar{t}}{\partial x^2}+\frac{\partial^2 \bar{t}}{\partial T^2}\right)\mathrm{d}\mathbf{A}=0. \tag{16}$$

Where δ_m in the subscript represents triangular diccretized elements.

5. Finite element method

Γ_0 use FEM, approximating under discussion variables $U(X,\ Y)$, $V(X,\ Y)$ and $\tilde{T}(X,\ Y)$ as U^m, V^n and $\tilde{T}^n$ for triangular elements A_n.

$$U\approx U^{\mathrm{m}}(X,\ Y)=\sum_{i=1}^{n} U_i^{\mathrm{m}}\Phi_i^{\mathrm{m}}(X,\ Y), \tag{17}$$

$$V\approx V^{\mathrm{m}}(X,\ Y)=\sum_{i=1}^{n} V_i^{\mathrm{m}}\Phi_i^{\mathrm{m}}(X,\ Y), \tag{18}$$

$$\tilde{T}\approx \tilde{T}^{\mathrm{m}}(X,\ Y)=\sum_{i=1}^{n} \tilde{T}_i^{\mathrm{m}}\Phi_i^{\mathrm{m}}(X,\ Y). \tag{19}$$

A six-nodal triangular element is represented by the function Φ_i^{m}, which is used to represent the test function. Substituting equation (14)-(16) into equation (17)-(19) to obtain the j-th equation used in the finite element method.

$$R_1^{(1)} = \sum_{i=1}^{n} \hat{U}_i^{\mathrm{m}} \int_{\Delta A^{\mathrm{m}}} \left(\sum_{i=1}^{n} \hat{U}_i^{\mathrm{m}} \Phi_i^{\mathrm{m}} \right) \frac{\partial \Phi_i^{\mathrm{m}}}{\partial x} + \left(\sum_{i=1}^{n} \hat{V}_i^{\mathrm{m}} \Phi_i^{\mathrm{m}} \right) \frac{\partial \Phi_i^{\mathrm{m}}}{\partial Y} \mathrm{d}A$$

$$- \gamma \left(\sum_{i=1}^{n} \hat{U}_i^{\mathrm{m}} \int_{\Delta A^{\mathrm{m}}} \frac{\partial \Phi_i^{\mathrm{m}}}{\partial x} \frac{\partial \Phi_i^{\mathrm{m}}}{\partial x} + \sum_{i=1}^{n} V_i^{\mathrm{m}} \int_{\Delta A^{\mathrm{m}}} \frac{\partial \Phi_i^{\mathrm{m}}}{\partial x} \frac{\partial \Phi_i^{\mathrm{m}}}{\partial Y} \right) \mathrm{d}A \tag{20}$$

$$- \frac{1}{Re} \sum_{i=1}^{n} \hat{U}_i^{\mathrm{m}} \int_{\Delta A^{\mathrm{m}}} \left(\frac{\partial \Phi_i^{\mathrm{m}}}{\partial x} \frac{\partial \Phi_i^{\mathrm{m}}}{\partial x} + \frac{\partial \Phi_i^{\mathrm{m}}}{\partial Y} \frac{\partial \Phi_i^{\mathrm{m}}}{\partial Y} \right) \mathrm{d}A,$$

$$R_1^{(2)} = \sum_{i=1}^{n} V_i^{\mathrm{m}} \int_{\Delta A^{\mathrm{m}}} \left(\sum_{i=1}^{n} \hat{U}_i^{\mathrm{m}} \Phi_i^{\mathrm{m}} \right) \frac{\partial \Phi_i^{\mathrm{m}}}{\partial x} + \left(\sum_{i=1}^{n} V_i^{\mathrm{m}} \Phi_i^{\mathrm{m}} \right) \frac{\partial \Phi_i^{\mathrm{m}}}{\partial Y} \mathrm{d}A$$

$$- \gamma \left(\sum_{i=1}^{n} V_i^{\mathrm{m}} \int_{\Delta A^{\mathrm{m}}} \frac{\partial \Phi_i^{\mathrm{m}}}{\partial y} \frac{\partial \Phi_i^{\mathrm{m}}}{\partial x} + \sum_{i=1}^{n} V_i^{\mathrm{m}} \int_{\Delta A^{\mathrm{m}}} \frac{\partial \Phi_i^{\mathrm{m}}}{\partial y} \frac{\partial \Phi_i^{\mathrm{m}}}{\partial Y} \right) \mathrm{d}A \tag{21}$$

$$- \frac{1}{Re} \sum_{i=1}^{n} V_i^{\mathrm{m}} \int_{\Delta A^{\mathrm{m}}} \left(\frac{\partial \Phi_i^{\mathrm{m}}}{\partial x} \frac{\partial \Phi_i^{\mathrm{m}}}{\partial x} + \frac{\partial \Phi_i^{\mathrm{m}}}{\partial Y} \frac{\partial \Phi_i^{\mathrm{m}}}{\partial Y} \right) \mathrm{d}A$$

$$- \frac{\alpha_1}{Re^3} \int_{\Delta A^{\mathrm{m}}} \sum_{i=1}^{n} \tilde{T}_i^{\mathrm{m}} \Phi_i^{\mathrm{m}} \mathrm{d}A,$$

$$R_1^{(3)} = \sum_{i=1}^{n} \tilde{T}_i^{\mathrm{m}} \int_{\Delta A^{\mathrm{m}}} \left(\sum_{i=1}^{n} \hat{U}_i^{\mathrm{m}} \Phi_i^{\mathrm{m}} \right) \frac{\partial \Phi_i^{\mathrm{m}}}{\partial x} + \left(\sum_{i=1}^{n} V_i^{\mathrm{m}} \Phi_i^{\mathrm{m}} \right) \frac{\partial \Phi_i^{\mathrm{m}}}{\partial Y} \mathrm{d}A \tag{22}$$

$$- \frac{1}{RePr} \sum_{i=1}^{n} \tilde{T}_i^{\mathrm{m}} \int_{\Delta A^{\mathrm{m}}} \left(\frac{\partial \Phi_i^{\mathrm{m}}}{\partial x} \frac{\partial \Phi_i^{\mathrm{m}}}{\partial x} + \frac{\partial \Phi_i^{\mathrm{m}}}{\partial Y} \frac{\partial \Phi_i^{\mathrm{m}}}{\partial Y} \right) \mathrm{d}A.$$

5.1 *Newton method*

After solving the above integrals by numerical integrations, we have a large system of equations to solve using Newton-Raphson form as:

$$J(b^e - b^{e+1}) - R(b^{(e)}) = 0. \tag{23}$$

The linear system is solved for index b, and the residual vector $R(b^{(e)})$ and Jacobian $J(b^{(e)})$ computed via divided differences from $\partial R/\partial(T, U, V)$.

5.2 *Computation of nusselt number*

The ratio of convective to conductive heat transfer is known as the Nusselt number (Nu), and it is a crucial parameter in thermal engineering that measures heat transfer efficiency.

$$Nu = -\frac{\partial T}{\partial n}, \tag{24}$$

where n is the normal direction to the plane.

The local Nusselt number at vertical wall is defined as

$$Nu = -\sum_{i=1}^{6} \tilde{T}_i^{\mathrm{m}} \frac{\partial \Phi_i^{\mathrm{m}}}{\partial x}. \tag{25}$$

The local Nusselt number at the horizontal wall is defined as

$$Nu = -\sum_{i=1}^{6} \tilde{T}_i^{\mathrm{m}} \frac{\partial \Phi_i^{\mathrm{m}}}{\partial y}. \tag{26}$$

The average Nusselt number on vertical and horizontal walls has the following relationships:

$$\overline{Nu} = \frac{1}{L}\int_0^L Nu\,\mathrm{d}Y, \quad \overline{Nu} = \frac{1}{L}\int_0^L Nu\,\mathrm{d}X. \tag{27}$$

6. Discussion

The mixed convection heat transfer inside a rectangular chamber is analyzed here for the governing equation [45]. The four lateral obstacles affect the flow and heat transfer characteristics. To streamline our own to achieve overshooting physical parameters, often the two circular branches represent an extremely degenerate flow. The cavity corresponding to $1 \leq Re \leq 50$ and $10^3 \leq Gr \leq 10^5$ is graphicaly described. First we fix the $Re = 50$ and varies Grashof number from 10^3 to 10^5. The geometrical properties were evaluated at fixed Prandtl number ($Pr = 0.71$), that corresponds to air. We ran additional carefully distributed flow ($Pr = 0.70$), ($Pr = 0.75$) ($Pr = 1.0$). Accordingly, we initially verified that the total rotational heat emitted from gravity.

Prandtl numbers improve the thickness of the thermal boundary layer and somewhat raise the Nusselt number. COMSOL Multiphysics was used to run the simulations using an Intel *i*7 CPU and 16 GB of RAM. It took around 2-5 minutes for each simulation to converge for the biggest mesh taken into consideration (20,000 elements). Although the approach is still effective up to the ranges that were studied ($Re \leq 50,\ Gr \leq 10^5$), we see that the computational cost increases as the Grashof/Reynolds numbers grow because finer meshes and stricter convergence tolerances are required.

Throughout the investigation, laminar flow accelerates are continuously varying in the Reynolds number ($Re = 50$). Because surpassing it would result in a shift to turbulent flow, which brings complicated, chaotic fluid motion, this upper limit is tightly enforced. A radically different and more intricate set of equations, such as those involving Reynolds-Averaged Navier-Stokes (RANS) models, are needed to simulate turbulence. Turbulent modeling is unable the predominant target and alignment of the control map becomes less based on the assumptions of laminar flow.

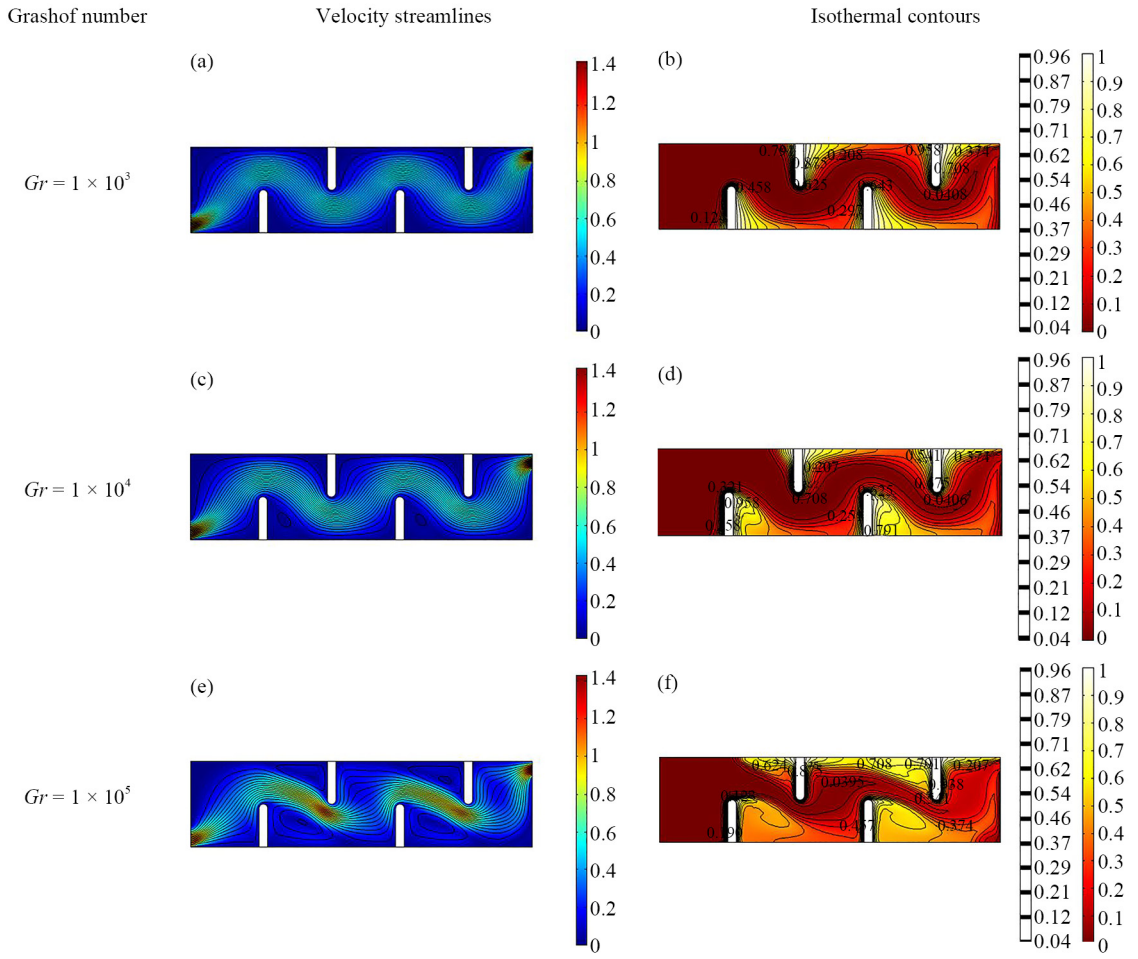

Figure 3. Streamlines and isothermal contours at $Re = 50$ for various grashof number

We see for Figures 3-4 the streamlines are vary near to each other and disturbing only at obstacle A, B, C and D in cavity and any other change not be seen in the cavity. In Figure for the grashof 1e5 the streamlines are much around the obstacle and at the left top and right bottom corner. Figure 3d, e heat transmission rate between obstacle A and B for $Gr = 10^3$ and $Gr = 10^4$ is slow. For Figure 3f the temperature gradiant is higher and maximum heat transfer observed. Also from graphically observed that heat transmission rate are approximately same for $Gr = 10^3$ and $Gr = 10^4$ in cavity but for 10^5 the heat transfer rate in much more than 10^3 and 10^4. A higher value of Grashof number causes fluid motion to accelerate as well as rate of convective heat transfer to upsurge. The dominant buoyancy at low Reynolds numbers $Re = 1 - 10$ causes weak flow with limited recirculating vortices close to the hot obstructions and corners. Inertial effects become important as the Reynolds number rises above 50. Deeper penetration by the entering fluid stream breaks up thermal plumes and creates bigger circulation cells that line up with the inlet-outlet flow. The location of barriers is crucial; those close to the outlet thin the thermal boundary layer, while those close to the entrance create greater wake vortices. For $Re = 10$ and different value of Grashof the streamline for velocity and isotherms for temperature observed in Figure 4. As a result, streamlines become parallel and the flow is fully settled at exit. And no circulation cells formed. In Figure 4b circulation of cells occurs near the obstacle and at right bottom corner, streamlines spread more between obstacle B and C. In Figure 4c the recirculating cells are high generated around the obstacle and other part of the cavity. For isotherms in Figure 4 d, e, f temperature gradient is more high for every next case. For $Re = 1$ and variation in Grashof number the corresponding streamline and isotherms are plotted in Figure 5. In Figure 5a the streamline are circulating

before the obstacle A and right bottom of the cavity. The streamlines are vary narrow at obstacle A and D. Figure 5b the circulation of cells at first part and last part of cavity is vary high as compare to middle part. In Figure 5c the circulation of cells made at the whole cavity. For isotherms the temperature gradient is vary high between the obstacle A, B, C and D. The maximum high temperature fluid out of the outlet, and Figure 5e, f also the temperature vary high between obstacles B and D but the fluid twat out has less temperature than Figure 5d. Small Reynolds numbers and large Grashof numbers produce far more complicated flow fields that involve separation and vortices near the channel walls, which have not yet been fully investigated. The behavior of velocity streamline and temperature distribution is observed graphically in Figures 6-8. In which for different values of *Re* we examine the behavior of *Gr* (see Figures 4 and 5).

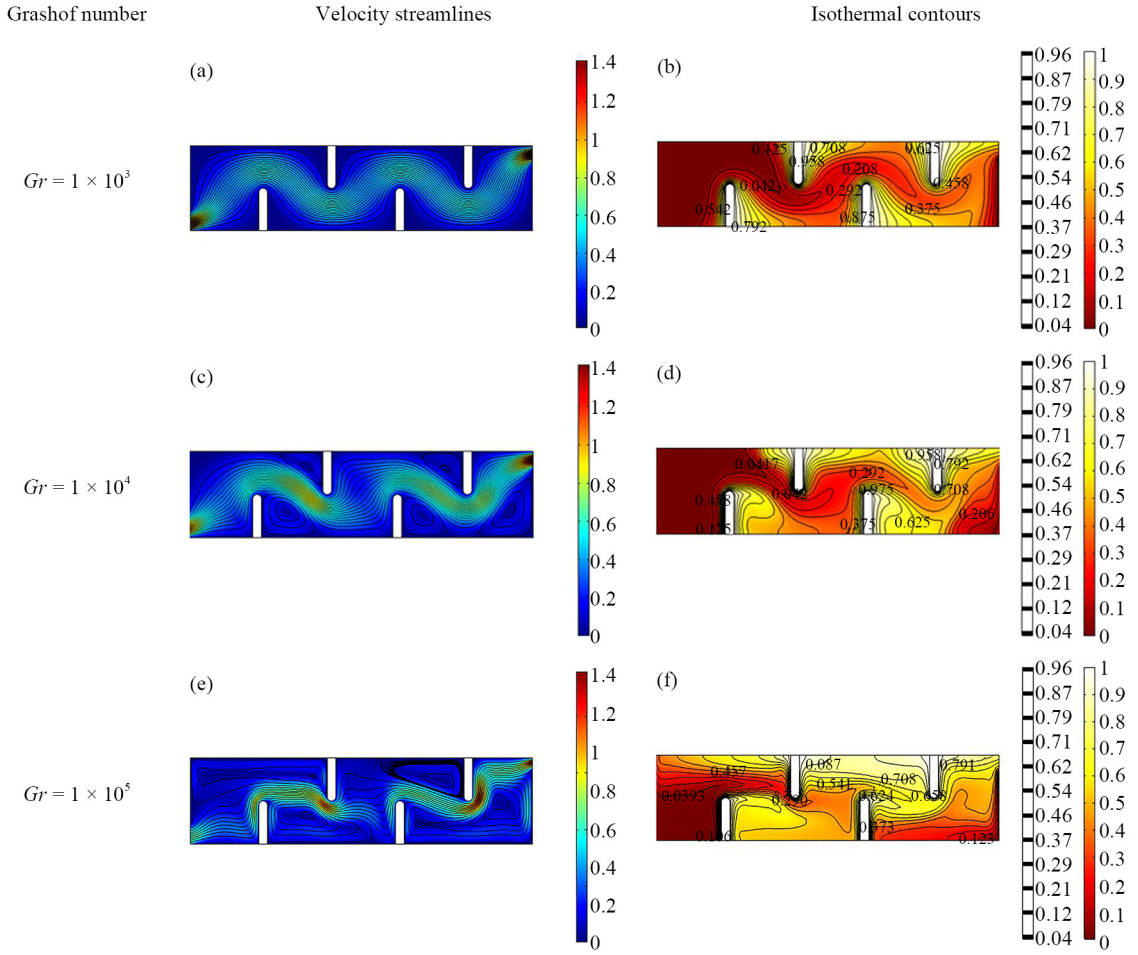

Figure 4. Streamlines and isothermal contours at $Re = 10$ for various grashof number

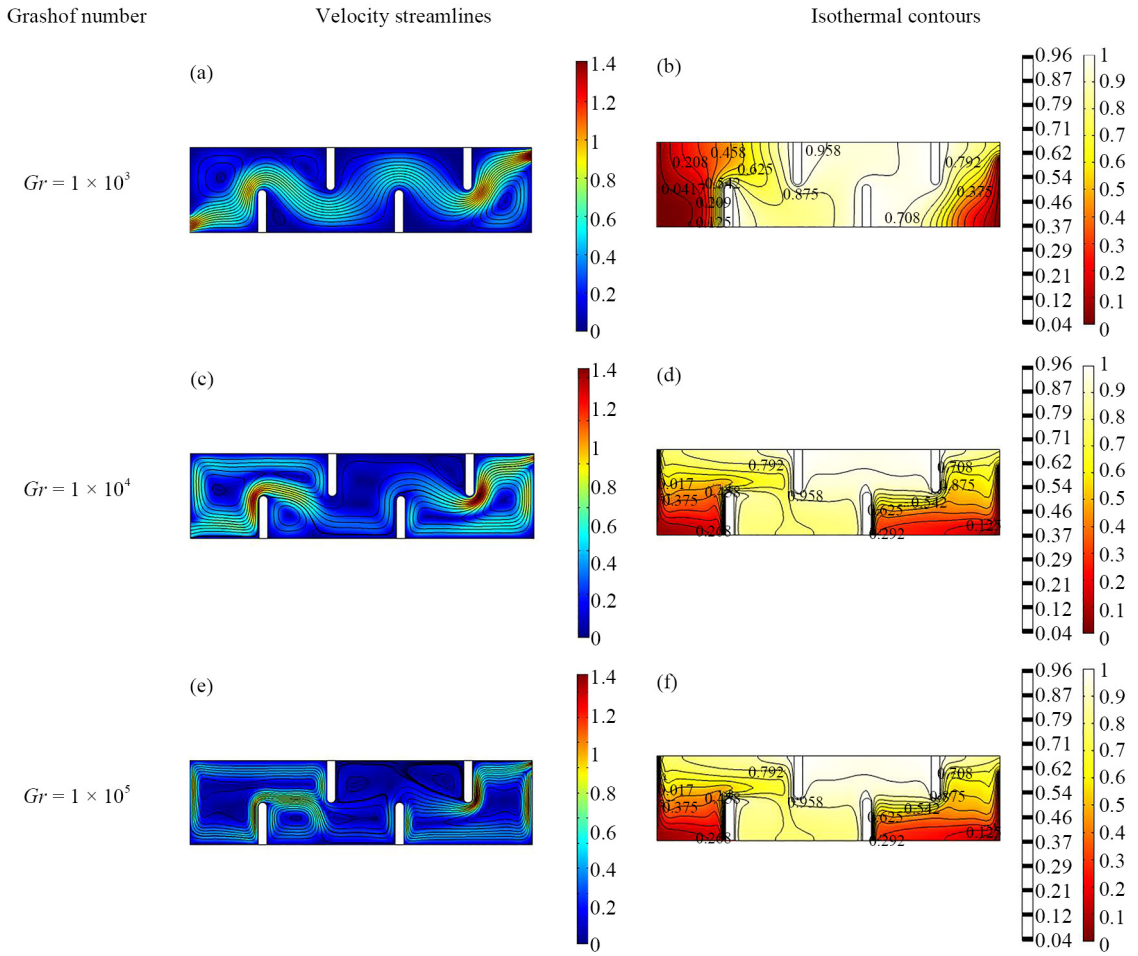

Figure 5. Streamlines and isothermal contours at $Re = 1$ for various grashof number

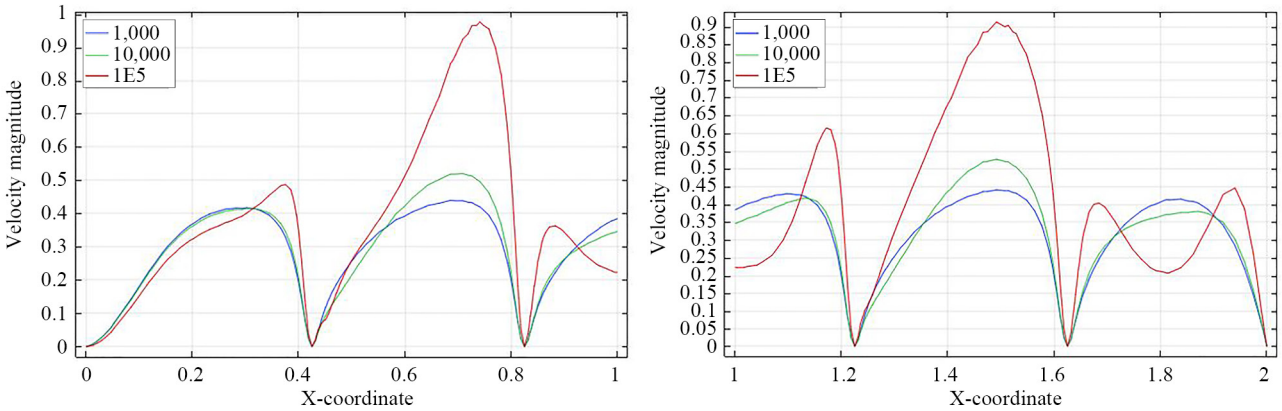

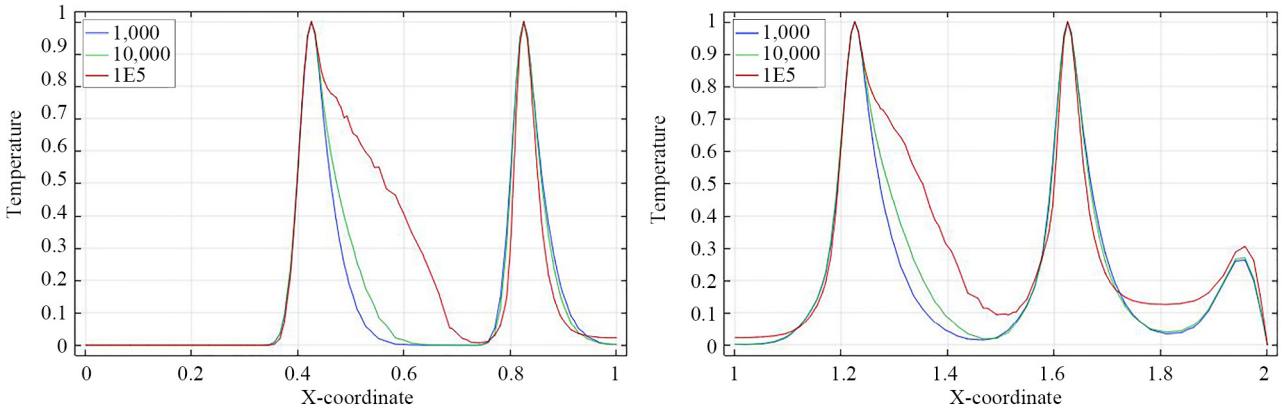

Figure 6. Velocity and temperature profile against different value of Gr and $Re = 50$

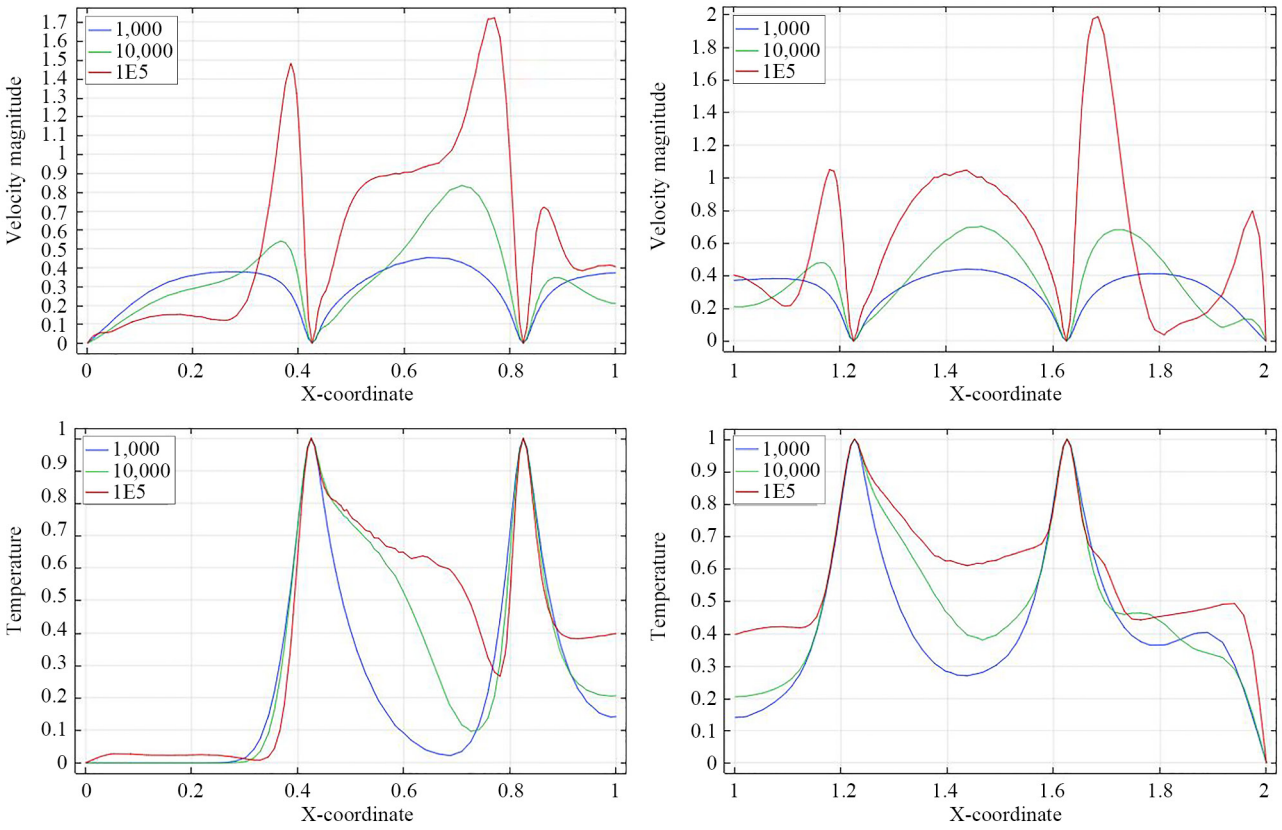

Figure 7. Velocity and temperature profile against different value of Gr and $Re = 10$

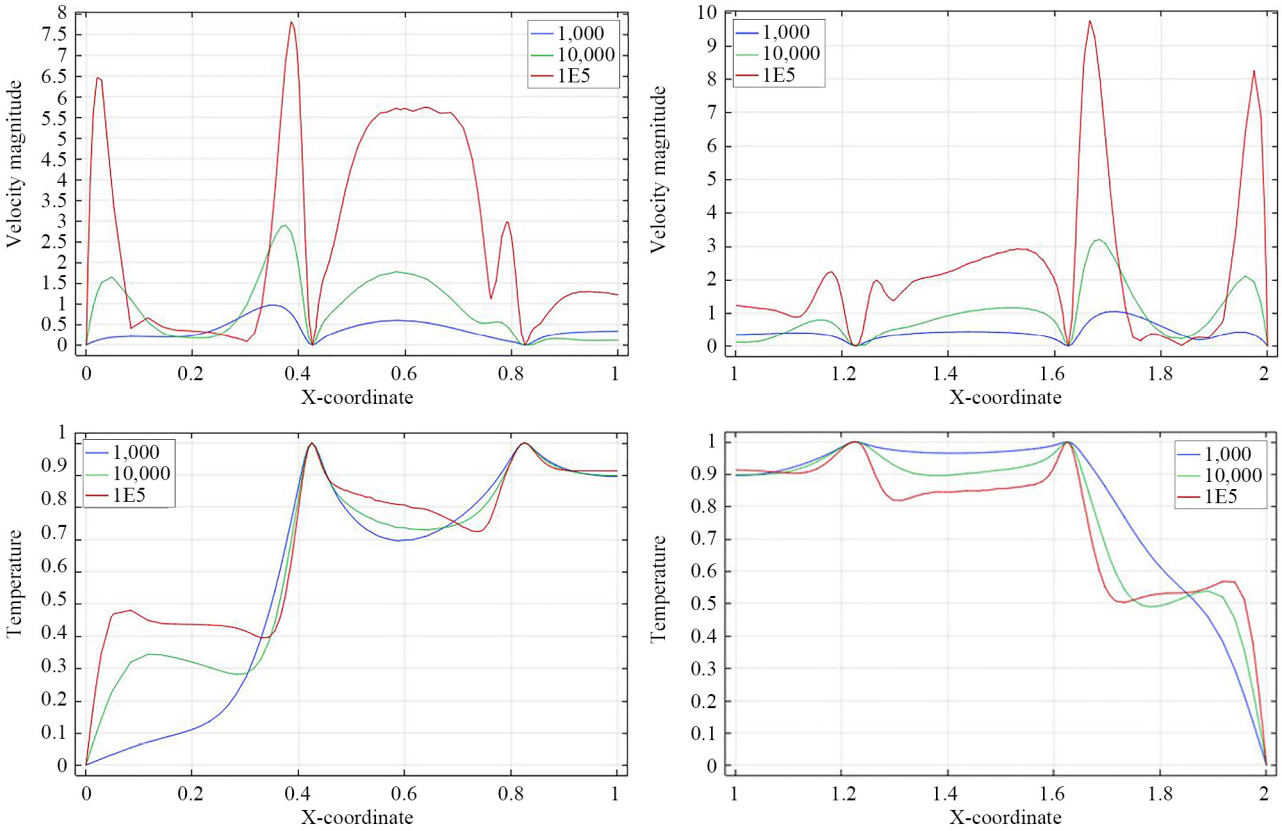

Figure 8. Velocity and temperature profile against different value of *Gr* and $Re = 1$

6.1 *Nusselt number*

Table 1. Variation of nusselt number with reynolds and grashof numbers

Reynolds number	Grashof number	Nusselt number
$Re = 50$	1,000	8.9047
	10,000	9.5339
	100,000	14.5171
$Re = 10$	1,000	5.2101
	10,000	6.2883
	100,000	9.7900
$Re = 1$	1,000	1.3302
	10,000	2.3928
	100,000	4.7407

Convective heat transfer between a solid surface and a surrounding fluid is measured by the Nusselt number (*Nu*). The calculated *Nu* values for various Grashof numbers (*Gr*) in fixed Reynolds numbers (*Re*) are shown in Table 1. *Nu* rises as Gr increases at $Re = 50$, indicating improved heat transfer under more powerful buoyancy effects. Although at

lower absolute levels due to lessened inertial pressures, *Nu* again exhibits a gradual rise when *Re* is lowered to 10 (and even to 1) while changing *Gr*. This demonstrates that, for all investigated *Re* values, *Nu* increases monotonically with *Gr* and that higher *Re* regimes maintain higher heat transfer rates.

7. Conclusion

In order to assess the mixed convection flow inside a rectangular enclosure with vertical heat-generating barriers, we performed a computer analysis. The flow rates in the rectangular chamber were given Reynolds values between 1 and 50. Heat transmission and streamlines in the presence of heated obstructions were the main topics of the study. The Reynolds number had a major impact on the flow patterns and temperature distribution in the mixed convection model. We found that when the Reynolds number rose, the streamlines' buoyancy-induced vortices grew, and the thermal layers close to the heated surfaces grew thinner and more concentrated. Higher Reynolds numbers were associated with an increase in the average Nusselt number at heated surfaces, indicating improved heat transfer. Furthermore, we discovered that substantial recirculation zones developed close to the barriers, whereas velocity distributions widened at higher Reynolds numbers. Reynolds and Grashof numbers interacted significantly to affect velocity fields and heat transfer characteristics at the inlet, outflow, and within the hollow. Fourier's law of conduction controlled the heat transfer, while the Navier-Stokes equations controlled the fluid dynamics. As Reynolds numbers rose, the flow generally showed significantly two-dimensional behavior, with clear vortical structures forming inside the hollow. The design and optimization of heat transfer systems in engineering applications may benefit from these findings, which provide insightful information on how heated impediments regulate thermal performance. To represent the transitory impacts of mixed convection in enclosures with numerous heated barriers, this work may be expanded to more complicated geometries, turbulent regimes, and time-dependent simulations in future research. Furthermore, adding magnetic field effects, porous media, or nanofluids would offer a more comprehensive understanding of the advanced thermal management applications in process engineering, solar energy systems, and electronic cooling.

Conflict of interest

The authors declare no competing financial interest.

References

[1] Guo G, Sharif MA. Mixed convection in rectangular cavities at various aspect ratios with moving isothermal sidewalls and constant flux heat source on the bottom wall. *International Journal of Thermal Sciences*. 2004; 43(5): 465-475. Available from: https://doi.org/10.1016/j.ijthermalsci.2003.08.008.

[2] Selimefendigil F, Öztop HF. Mixed convection in a partially heated triangular cavity filled with nanofluid having a partially flexible wall and internal heat generation. *Journal of the Taiwan Institute of Chemical Engineers*. 2017; 70: 168-178. Available from: https://doi.org/10.1016/j.jtice.2016.10.038.

[3] Haq RU, Soomro FA, Mekkaoui T, Al-Mdallal QM. MHD natural convection flow enclosure in a corrugated cavity filled with a porous medium. *International Journal of Heat and Mass Transfer*. 2018; 121: 1168-1178. Available from: https://doi.org/10.1016/j.ijheatmasstransfer.2018.01.063.

[4] Gangawane KM, Oztop HF, Ali ME. Mixed convection in a lid-driven cavity containing triangular block with constant heat flux: Effect of location of block. *International Journal of Mechanical Sciences*. 2019; 152: 492-511. Available from: https://doi.org/10.1016/j.ijmecsci.2019.01.020.

[5] Shah SS, Haq RU, Al-Kouz W. Mixed convection analysis in a split lid-driven trapezoidal cavity having elliptic shaped obstacle. *International Communications in Heat and Mass Transfer*. 2021; 126: 105448. Available from: https://doi.org/10.1016/j.icheatmasstransfer.2021.105448.

[6] Moallemi MK, Jang KS. Prandtl number effects on laminar mixed convection heat transfer in a lid-driven cavity. *International Journal of Heat and Mass Transfer*. 1992; 35(8): 1881-1892. Available from: https://doi.org/10.1016/0017-9310(92)90191-T.

[7] Prasad AK, Koseff JR. Combined forced and natural convection heat transfer in a deep lid-driven cavity flow. *International Journal of Heat and Fluid Flow*. 1996; 17(5): 460-467. Available from: https://doi.org/10.1016/0142-727X(96)00054-9.

[8] Khanafer KM, Chamkha AJ. Mixed convection flow in a lid-driven enclosure filled with a fluid-saturated porous medium. *International Journal of Heat and Mass Transfer*. 1999; 42(13): 2465-2481. Available from: https://doi.org/10.1016/S0017-9310(98)00227-0.

[9] Basak T, Roy S, Sharma PK, Pop I. Analysis of mixed convection flows within a square cavity with uniform and non-uniform heating of bottom wall. *International Journal of Thermal Sciences*. 2009; 48(5): 891-912. Available from: https://doi.org/10.1016/j.ijthermalsci.2008.08.003.

[10] Nadeem S, Alblawi A, Muhammad N, Alarifi IM, Issakhov A, Mustafa MT. A computational model for suspensions of motile micro-organisms in the flow of ferrofluid. *Journal of Molecular Liquids*. 2020; 298: 112033. Available from: https://doi.org/10.1016/j.molliq.2019.112033.

[11] Oztop HF, Dagtekin I. Mixed convection in two-sided lid-driven differentially heated square cavity. *International Journal of Heat and Mass Transfer*. 2004; 47(8-9): 1761-1769. Available from: https://doi.org/10.1016/j.ijheatmasstransfer.2003.10.016.

[12] Alblawi A, Keyani S, Nadeem S, Issakhov A, Alarifi IM. Ciliary flow of Casson nanofluid with the influence of MHD having carbon nanotubes. *Current Nanoscience*. 2021; 17(3): 447-462. Available from: https://doi.org/10.2174/1573413716999201015090335.

[13] Ullah N, Nadeem S, Khan AU. Finite element simulations for natural convective flow of nanofluid in a rectangular cavity having corrugated heated rods. *Journal of Thermal Analysis and Calorimetry*. 2021; 143(6): 4169-4181. Available from: https://doi.org/10.1007/s10973-020-09378-4.

[14] Alsabery AI, Armaghani T, Chamkha AJ, Hashim I. Two-phase nanofluid model and magnetic field effects on mixed convection in a lid-driven cavity containing heated triangular wall. *Alexandria Engineering Journal*. 2020; 59(1): 129-148. Available from: https://doi.org/10.1016/j.aej.2019.12.017.

[15] Alblawi A, Malik MY, Nadeem S, Abbas N. Buongiorno's nanofluid model over a curved exponentially stretching surface. *Processes*. 2019; 7(10): 665. Available from: https://doi.org/10.3390/pr7100665.

[16] Khan WA, Khan ZH. Mixed convection of single-walled carbon nanotubes in a triangular cavity containing a pentagonal impediment. In: *IOP Conference Series: Materials Science and Engineering*. Vol. 37. UK: IOP Publishing Ltd; 2020. Available from: https://doi.org/10.1088/1757-899X/839/1/012021.

[17] Xiong PY, Hamid A, Iqbal K, Irfan M, Khan M. Numerical simulation of mixed convection flow and heat transfer in the lid-driven triangular cavity with different obstacle configurations. *International Communications in Heat and Mass Transfer*. 2021; 123: 105202. Available from: https://doi.org/10.1016/j.icheatmasstransfer.2021.105202.

[18] Khan ZH, Hamid M, Khan WA, Sun L, Liu H. Thermal non-equilibrium natural convection in a trapezoidal porous cavity with heated cylindrical obstacles. *International Communications in Heat and Mass Transfer*. 2021; 126: 105460. Available from: https://doi.org/10.1016/j.icheatmasstransfer.2021.105460.

[19] Nikan O, Avazzadeh Z, Machado JT. Numerical treatment of microscale heat transfer processes arising in thin films of metals. *International Communications in Heat and Mass Transfer*. 2022; 132: 105892. Available from: https://doi.org/10.1016/j.icheatmasstransfer.2022.105892.

[20] Usman M, Khan ZH, Liu MB. MHD natural convection and thermal control inside a cavity with obstacles under the radiation effects. *Physica A: Statistical Mechanics and Its Applications*. 2019; 535: 122443. Available from: https://doi.org/10.1016/j.physa.2019.122443.

[21] Haq RU, Soomro FA, Wang X, Tlili I. Partially heated lid-driven flow in a hexagonal cavity with inner circular obstacle via FEM. *International Communications in Heat and Mass Transfer*. 2020; 117: 104732. Available from: https://doi.org/10.1016/j.icheatmasstransfer.2020.104732.

[22] Abdelmalek Z, Tayebi T, Dogonchi AS, Chamkha AJ, Ganji DD, Tlili I. Role of various configurations of a wavy circular heater on convective heat transfer within an enclosure filled with nanofluid. *International Communications in Heat and Mass Transfer*. 2020; 113: 104525. Available from: https://doi.org/10.1016/j.icheatmasstransfer.2020.104525.

[23] Nikan O, Avazzadeh Z, Machado JT, Rasoulizadeh MN. An accurate localized meshfree collocation technique for the telegraph equation in propagation of electrical signals. *Engineering with Computers*. 2023; 39(3): 2327-2344. Available from: https://doi.org/10.1007/s00366-022-01630-9.

[24] Rehman KU, Al-Mdallal QM, Tlili I, Malik MY. Impact of heated triangular ribs on hydrodynamic forces in a rectangular domain with heated elliptic cylinder: Finite element analysis. *International Communications in Heat and Mass Transfer*. 2020; 112: 104501. Available from: https://doi.org/10.1016/j.icheatmasstransfer.2020.104501.

[25] Kargarsharifabad H. Optimization of arrangement of conducting fins and insulated obstacles inside a cavity: The couple of numerical solutions and genetic algorithm methods. *Journal of Thermal Analysis and Calorimetry*. 2020; 147: 421-433. Available from: https://doi.org/10.1007/s10973-020-10276-y.

[26] Li M, Nikan O, Qiu W, Xu D. An efficient localized meshless collocation method for the two-dimensional Burgers-type equation arising in fluid turbulent flows. *Engineering Analysis with Boundary Elements*. 2022; 144: 44-54. Available from: https://doi.org/10.1016/j.enganabound.2022.08.007.

[27] Ullah I, Arif M, Nadeem S, Alzabut J. Numerical computations of MHD mixed convection flow of Bingham fluid in a porous square chamber with a wavy cylinder. *International Journal of Thermofluids*. 2024; 24: 100938. Available from: https://doi.org/10.1016/j.ijft.2024.100938.

[28] Ullah I, Ullah H, Nadeem S, Alzabut J, Saleem S, Alblawi A. Inclined MHD mixed convection of a Bingham fluid in a lid-driven square cavity with an embedded wavy cylinder: Thermal and magnetic field interactions. *Journal of Thermal Analysis and Calorimetry*. 2025; 150: 10105-10126. Available from: https://doi.org/10.1007/s10973-025-14279-5.

[29] Bibi A, Ullah N, Nadeem S. Nanofluid magnetoconvection and entropy generation: A computational study for water treatment and resource management. *Applied Water Science*. 2025; 15: 64. Available from: https://doi.org/10.1007/s13201-025-02403-7.

[30] Khan ZH, Khan WA, Hamid M, Liu H. Finite element analysis of hybrid nanofluid flow and heat transfer in a split lid-driven square cavity with Y-shaped obstacle. *Physics of Fluids*. 2020; 32(9): 093609. Available from: https://doi.org/10.1063/5.0021638.

[31] Ibtesam M, Nadeem S, Alzabut J. Numerical treatment of magnetohydrodynamic flow of nanofluids through free convection in a hexagonal-complex-shaped cavity having an embedded heated fin. *Journal of Thermal Analysis and Calorimetry*. 2025; 150: 4483-4502. Available from: https://doi.org/10.1007/s10973-025-14019-9.

[32] Wang CH, Feng YY, Yue K, Zhang XX. Discontinuous finite element method for combined radiation-conduction heat transfer in participating media. *International Communications in Heat and Mass Transfer*. 2019; 108: 104287. Available from: https://doi.org/10.1016/j.icheatmasstransfer.2019.104287.

[33] Nadeem S, Siddiqua A, Alzabut J. Flow of SWCNT and MWCNT based hybrid nanofluids in a semi-circular enclosure with corrugated wall. *Advances in Mechanical Engineering*. 2025; 17(1): 16878132251314272.

[34] Soomro FA, Hammouch Z. Heat transfer analysis of CuO-water enclosed in a partially heated rhombus with heated square obstacle. *International Journal of Heat and Mass Transfer*. 2018; 118: 773-784. Available from: https://doi.org/10.1016/j.ijheatmasstransfer.2017.11.043.

[35] Ullah N, Lu D, Nadeem S. Enhancing thermal performance in enclosures filled with nanofluids subjected to sinusoidal heating: A numerical study. *Engineering Applications of Computational Fluid Mechanics*. 2024; 18(1): 2338522. Available from: https://doi.org/10.1080/19942060.2024.2338522.

[36] Ibtesam M, Nadeem S, Alzabut J. Numerical computations of magnetohydrodynamic mixed convective flow of Casson nanofluid in an open-ended cavity formed by earthquake-induced faults. *Applied Mathematics and Mechanics*. 2024; 45(12): 2215-2230. Available from: https://doi.org/10.1007/s10483-024-3190-9.

[37] Mourad A, Aissa A, Mebarek-Oudina F, Jamshed W, Ahmed W, Ali HM, et al. Galerkin finite element analysis of thermal aspects of Fe_3O_4-MWCNT/water hybrid nanofluid filled in wavy enclosure with uniform magnetic field effect. *International Communications in Heat and Mass Transfer*. 2021; 126: 105461. Available from: https://doi.org/10.1016/j.icheatmasstransfer.2021.105461.

[38] Nadeem S, Hamed YS, Riaz MB, Ullah I, Alzabut J. Finite element method for natural convection flow of Casson hybrid (Al_2O_3-Cu/water) nanofluid inside H-shaped enclosure. *AIP Advances*. 2024; 14(8): 085130. Available from: https://doi.org/10.1063/5.0218934.

[39] Nadeem S, Akber R, Ghazwani HA, Alzabut J, Hassan AM. Numerical computations for convective MHD flow of viscous fluid inside the hexagonal cavity having sinusoidal heated walls. *Results in Physics*. 2024; 56: 107229. Available from: https://doi.org/10.1016/j.rinp.2023.107229.

[40] Nadeem S, Salma R, Ullah N, Alzabut J, Ghazwani HA. Numerical solutions for MHD mixed convection flow in a square wavy cavity inside heated corrugated rods. *International Communications in Heat and Mass Transfer*. 2023; 149: 107136. Available from: https://doi.org/10.1016/j.icheatmasstransfer.2023.107136.

[41] Zhao B, Chen H, Gao D, Xu L, Zhang Y. Heat transfer simulation in cavity of twin screw compressor under coupling of clearance leakage-heat by utilizing fuzzy beamlet finite element model. *Journal of Thermal Analysis and Calorimetry*. 2021; 143(4): 3221-3232. Available from: https://doi.org/10.1007/s10973-020-09531-z.

[42] Nadeem S, Akber R, Ghazwani HA, Alzabut J. FEM-based numerical solutions for mixed convection MHD flow of fluid inside the square cavity having sinusoidal walls. *Numerical Heat Transfer, Part A: Applications*. 2025; 86(5): 1021-1047. Available from: https://doi.org/10.1080/10407782.2023.2270151.

[43] Akram B, Ullah N, Nadeem S, Eldin SM. Simulations for MHD mixed convection in a partially heated lid-driven chamfered enclosure. *Numerical Heat Transfer, Part A: Applications*. 2024; 85(22): 3821-3841. Available from: https://doi.org/10.1080/10407782.2023.2242581.

[44] Nadeem S, Arif M, Ullah I, Alzabut J. MHD natural convection of nanofluid flow using a corrugated permeable medium within corrugated circular cavity. *Journal of Thermal Analysis and Calorimetry*. 2025; 150: 5697-5724. Available from: https://doi.org/10.1007/s10973-025-14032-y.

[45] Batchelor GK. *An Introduction to Fluid Dynamics*. Cambridge: Cambridge University Press; 2000. Available from: https://doi.org/10.1017/CBO9780511800955.